



**HAL**  
open science

# Systematic generation of biophysically detailed models with generalization capability for non-spiking neurons

Loïs Naudin, Juan Luis Jiménez Laredo, Qiang Liu, Nathalie Corson

## ► To cite this version:

Loïs Naudin, Juan Luis Jiménez Laredo, Qiang Liu, Nathalie Corson. Systematic generation of biophysically detailed models with generalization capability for non-spiking neurons. 2021. hal-03474984

**HAL Id: hal-03474984**

**<https://hal.science/hal-03474984>**

Preprint submitted on 10 Dec 2021

**HAL** is a multi-disciplinary open access archive for the deposit and dissemination of scientific research documents, whether they are published or not. The documents may come from teaching and research institutions in France or abroad, or from public or private research centers.

L'archive ouverte pluridisciplinaire **HAL**, est destinée au dépôt et à la diffusion de documents scientifiques de niveau recherche, publiés ou non, émanant des établissements d'enseignement et de recherche français ou étrangers, des laboratoires publics ou privés.

# Systematic generation of biophysically detailed models with generalization capability for non-spiking neurons

Lois Naudin<sup>1\*</sup>, Juan Luis Jiménez Laredo<sup>2</sup>, Qiang Liu<sup>3</sup>, and Nathalie Corson<sup>1</sup>

<sup>1</sup>Normandie Univ, UNIHAVRE, LMAH, FR-CNRS-3335, ISCN, Le Havre 76600, France

<sup>2</sup>Normandie Univ, UNIHAVRE, LITIS, FR-CNRS-3638, ISCN, Le Havre 76600, France

<sup>3</sup>Lulu and Anthony Wang Laboratory of Neural Circuits and Behavior, The Rockefeller University, New York, United States

\*Corresponding author: lois.naudin@gmail.com

October 30, 2021

## Abstract

Unlike spiking neurons which compress continuous inputs into digital signals for transmitting information via action potentials, non-spiking neurons modulate analog signals through graded potential responses. Such neurons have been found in a large variety of nervous tissues in both vertebrates and invertebrates species, and proved to play a central role in neuronal information processing. If general and vast efforts have been made for many years to model spiking neurons using conductance-based models (CBMs), very few methods have been developed for non-spiking neurons. When a CBM is built to characterize the neuron behavior, it should be endowed with generalization capabilities (*i.e.* the ability to predict acceptable neuronal responses to different novel stimuli not used during the model's building). Yet, since CBMs contain a large number of parameters, it may typically suffer from a lack of such a capability. In this paper, we propose a new systematic approach based on multi-objective optimization which builds general non-spiking models with generalization capabilities. The proposed approach only requires macroscopic experimental data from which all the model parameters are simultaneously determined without compromise. Such an approach is applied on three non-spiking neurons of the nematode *Caenorhabditis elegans* (*C. elegans*), a well-known model organism in neuroscience that predominantly transmits information through non-spiking signals. These three neurons, named RIM, AIY and AFD, represent, to date, the three possible forms of non-spiking neuronal responses of *C. elegans*.

**Keywords:** Conductance-based neuron models; non-spiking neurons; generalization capability; multi-objective optimization; *Caenorhabditis elegans*.

## Author Summary

Neurons are fundamental cells of the nervous system sending signals rapidly and precisely to other cells in response to a stimulus. They can be of different sizes, of different shapes, and in the great diversity of neurons, there are two types of behavior: *spiking* and *non-spiking*. The amplitude and waveform of a spiking signal is essentially invariant with respect to the amplitude, duration, and waveform of the stimulus, unlike a non-spiking signal which is stimulus dependent. If much efforts have been made for many years to develop methods adapted for the modeling of spiking neurons given the ubiquity of such neurons in neuronal process, very few for the non-spiking ones. However, the latter have also been found in a large variety of nervous tissues in both vertebrates and invertebrates species, and they play a central role in information processing as well. Our work aims at proposing a method suited for the modeling of non-spiking neurons,

with a particular focus on the generalization capability of the model. This capability corresponds to the ability of the model to fit additional data or predict future observations reliably, which is a paramount feature that any model should have whatever the field considered.

## 1 Introduction

Spiking neurons are often considered as the major information processing unit of the nervous system. Nonetheless, not all neurons elicit spikes. While spiking neurons compress continuous inputs into digital signals for transmitting information via action potentials, non-spiking neurons modulate analog signals through graded potential responses. An advantage of this type of response is that it allows not to sacrifice information content [75]. A large variety of nervous tissues in both vertebrates and invertebrates species have revealed that a number of sensory, inter and motoneurons function without eliciting spikes. Some examples are the human retina neurons [40], numerous interneurons in insects and crustaceans [68], the motoneurons of the *Ascaris* worm [14, 15], or most of the *C. elegans* neurons [28]. Non-spiking neurons have been found in sensorimotor and central pattern generator circuits, proved to be central in neuronal integration [68] and to provide a determining mechanism for the control of motor behavior [10, 46, 45]. As far as we know, very few modeling efforts have been carried out to characterize this type of neurons' behavior using conductance-based models (CBMs).

CBMs have become one of the most powerful computational approaches for characterizing the behavior of neurons [3, 59]. In simple terms, a CBM is a biophysical representation of a neuron in which the ion channels are represented by conductances and the polar membrane by a capacitor [16, 39]. In such models, every individual parameter and state variable have an established electrophysiological meaning so that their role in the neuron dynamics can be unequivocally identified. However, due to the difficulty to perform some experimental recordings (*e.g.* ionic conductances [73]), many modeling studies suffer from the lack of sufficient physiological data to determine all the parameter values. As a consequence, parameters are often tuned in an *ad-hoc* manner. Furthermore, when new biological recordings come into play, these models can typically suffer from good generalization capabilities (*i.e.* the ability to predict acceptable responses to stimuli not used while building the model) [21, 20]. In order to overcome these issues, we propose a new approach in which all the model parameters are simultaneously determined, from *macroscopic* data, by trading off the accuracy and the capability of generalization of the model.

To obtain a CBM that characterizes the neuron behavior accurately and with a good generalization capability, one needs to capture the right underlying bifurcation structure of the neuron, *i.e.* the qualitative changes that the neuron behavior undergoes as a result of a change in stimuli. In a sense, *neurons are dynamical systems* [36]. In this paper, we show that the steady-state current (depicted in Figure 1) plays a pivotal role in the dynamic of non-spiking CBMs by determining: (i) the number of equilibria as well as their values, and (ii) all the bifurcations of the resting state along with the values to which they occur. Therefore, this paper adopts a multi-objective optimization approach so that, in addition to fitting the membrane potential evolution, it also captures the underlying bifurcation structure of non-spiking neurons by considering an additional objective: the fitting of the steady-state current.

In the present work, we apply our proposed approach on three non-spiking neurons (RIM, AIY and AFD) of the nematode *C. elegans*. Non-spiking neurons can display two typical behaviors: (i) *near-linear*, with a smoothly depolarization or hyperpolarization from the resting potential, and (ii) *bistable*, with nonlinear transitions characterized by a voltage jump between the resting potential and a depolarized potential of higher voltage. In particular, RIM and AIY neurons display a near-linear behavior (Figure 1.A) while AFD exhibits a bistable one (Figure 1.B) so that our approach is applied on experimental behavior representative of the known types of non-spiking neurons.

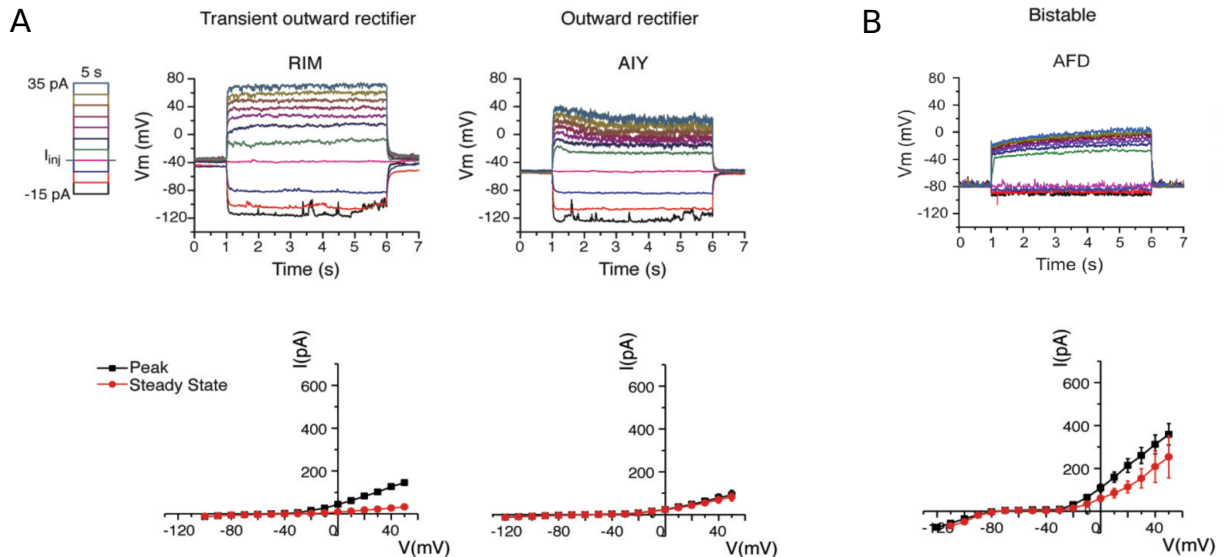


Figure 1: In-vivo recordings of three different non-spiking neurons of *C. elegans* which represent, to date, the three forms of possible non-spiking neuronal responses of the nematode. (Top) Evolution of membrane potential for a series of current injections, in spans of 5 seconds, starting from -15pA and increasing to 35pA by 5pA increments. (Bottom) I-V relationships obtained from averaged voltage-clamp recordings (RIM:  $n = 3$ ; AIY:  $n = 7$ ; AFD:  $n = 3$ ). Peak currents are measured by the absolute maximum amplitude of currents within the first 100 ms of each voltage step onset, while steady-state currents are measured by the averaged currents of the last 50 ms of each voltage step. (A) Near-linear behavior. Published in [51] (reproduced with the consent of the authors). (B) Bistable behavior. New unpublished results for AFD.

## 2 Materials and Methods

### 2.1 Electrophysiology

The *C. elegans* strain used was PY1322 *oyIs18[gcy-8::GFP]* X with GFP exclusively expressed in AFD neurons. Experiments were performed on young adult hermaphrodites (3-4 days old) maintained at room temperature (22-23°C) on nematode growth medium (NGM) plates seeded with *E. coli* OP50 bacteria as a food source [5]. Electrophysiological recording was performed as previously described [51]. Briefly, an adult was immobilized with cyanoacrylate adhesive (Vetbond tissue adhesive; 3M) on a Sylgard 184-coated (Dow Corning) glass coverslip and dissected to expose AFD. Recordings were performed using single-electrode whole-cell current clamp (Heka, EPC-10 USB) with two-stage capacitive compensation optimized at rest, and series resistance compensated to 50%. The standard pipette solution was (all concentrations in mM): [K-gluconate 115; KCl 15; KOH 10; MgCl<sub>2</sub> 5; CaCl<sub>2</sub> 0.1; Na<sub>2</sub>ATP 5; NaGTP 0.5; Na-cGMP 0.5; cAMP 0.5; BAPTA 1; Hepes 10; Sucrose 50], with pH adjusted with KOH to 7.2, osmolarity 320–330 mOsm. The standard extracellular solution was: [NaCl 140; NaOH 5; KCl 5; CaCl<sub>2</sub> 2; MgCl<sub>2</sub> 5; Sucrose 15; Hepes 15; Dextrose 25], with pH adjusted with NaOH to 7.3, osmolarity 330–340 mOsm. Liquid junction potentials were calculated and corrected before recording. Data analysis were conducted using Fitmaster (Heka) and exported to OriginPro 2018 (OriginLab) for graphing.

### 2.2 Conductance-based model description

Conductance-based neuron models, based on the Hodgkin-Huxley formalism, were first postulated in a series of seminal works in the 1950s [30, 31, 32, 33, 29]. They describe the neuronal dynamics in terms of activation and inactivation of voltage-gated conductances. In particular,

the dynamic of the membrane potential  $V$  is described by a general equation of the form

$$C \frac{dV}{dt} = - \sum_{ion} I_{ion} + I \quad (1)$$

where  $C$  is the membrane capacitance,  $\sum_{ion} I_{ion}$  is the total current flowing across the cell membrane, and  $I$  is an applied current.

The dynamics of every  $I_{ion}$  are governed by gating particles (gates) sensitive to the changes in the membrane potential (voltage). These gates can be of two types: activation gate and inactivation gate, each of which can be in an open or a closed state. The probability of an activation or inactivation gate being in the open state is denoted respectively by the variables  $m$  and  $h$ . Thus, the current generated by a large population of identical ion channels is given by

$$I_{ion} = g_{ion} m_{ion}^a h_{ion}^b (V - E_{ion})$$

where  $g_{ion}$  is the maximal conductance (namely the conductance of the channel when all the gates are open);  $E_{ion}$  is the reverse potential, that is, the potential at which the ion current reverses its direction (a.k.a. equilibrium potential); and  $a$  and  $b$  respectively refer to the number of activation and inactivation gates. Channels that do not have inactivation gates ( $b = 0$ ) induce a persistent current (*i.e.* current that does not inactivate) noted by  $I_{ion,p}$ , while channels that do inactivate ( $b = 1$ ) induce a transient current (*i.e.* current that inactivates) noted by  $I_{ion,t}$ .

The dynamics of variables  $m$  and  $h$  are described by the following equation:

$$\frac{dx}{dt} = \frac{x_{\infty}(V) - x}{\tau_x}, \quad x \in \{m, h\}. \quad (2)$$

where  $\tau_x$  is the *constant* time for which  $x$  reaches its respective equilibrium value  $x_{\infty}$ . The latter is expressed by a Boltzmann sigmoid function:

$$x_{\infty}(V) = \frac{1}{1 + \exp\left(\frac{V_{1/2}^x - V}{k_x}\right)}, \quad x \in \{m, h\}.$$

where  $V_{1/2}^x$  satisfies  $x_{\infty}(V_{1/2}^x) = 1/2$  and  $k_x$  is the slope factor with  $k_m > 0$  and  $k_h < 0$  as to represent activation and inactivation respectively, *i.e.*, smaller values of  $|k_x|$  lead to a sharper  $x_{\infty}$ .

In a previous work [59], a series of in-silico experiments were conducted for determining the most suitable models to the electrophysiology of *C. elegans* neurons:  $I_{Ca,p} + I_{Kir} + I_{K,t} + I_L$ -model was selected for RIM and AFD neurons, and  $I_{Ca,t} + I_{Kir} + I_{K,p} + I_L$ -model for AIY. A complete mathematical description of these models is presented in Appendix A.

### 2.3 Objective functions

**Primary objective: Membrane potential.** The primary objective of the proposed conductance-based models is to reproduce the evolution of the membrane potential depicted in Figure 1 for the different neurons under study. To that end, we employ the cost function  $f_V$  as being the root-mean-square error normalized to the noise level (*i.e.* standard deviation) of each experimental voltage trace. The noise level, noted  $\sigma_I$ , is estimated as in [81], that is, we choose a time window at the end of each trace where the curve is relatively flat for calculating the standard deviation. Therefore,  $f_V$  takes the following form:

$$f_V(\theta_V) = \frac{1}{|I|} \sum_I \frac{\sqrt{\frac{1}{N} \sum_t (V_{exp}(I, t) - V_{\theta_V}(I, t))^2}}{\sigma_I} \quad (3)$$

where  $V_{exp}(I, t)$  are the *experimental* voltages depicted in Figure 1 and  $V_{\theta_V}(I, t)$  the voltages *estimated* by the model where  $\theta_V$  is the vector containing all the model parameters (see Appendix A);  $t \in [0, 50ds]$  corresponds to the biological real time with a sampling period of  $\Delta t = 0.004ds$ ;  $N = 12500$  is the number of data points in the measurement record, and  $I$  corresponds to successive step values of current injections starting from -15pA and increasing to 35pA by intervals of 5pA.

**Secondary objective: Steady-state current.** As the primary objective alone may fail to predict generalized responses to novel stimuli, the secondary objective aims to fit the mean of the experimental responses of the steady-state current (RIM:  $n = 3$ ; AIY:  $n = 7$ ; AFD:  $n = 3$ ) displayed in Figure 1. The fitting of the steady-state current is carried out by minimizing the root-mean-square error normalized to the standard deviation, noted  $\sigma$ . Therefore, the cost function denoted  $f_\infty$  is defined as follows:

$$f_\infty(\theta_{SS}) = \frac{1}{|V_H|} \sum_{V_H} \frac{\sqrt{(I_\infty^{exp}(V_H) - I_\infty^{\theta_{SS}}(V_H))^2}}{\sigma_{V_H}} \quad (4)$$

where  $I_\infty^{exp}(V)$  is the *experimental* mean (Figure 1) and  $I_\infty^{\theta_{SS}}(V)$  the *estimated* one;  $\theta_{SS}$  is the vector containing the parameters related to the steady-state current (see Appendix A);  $V_H$  corresponds to a series of voltage clamped starting from -100mV and increasing to 50mV by 10mV increments, and  $\sigma_{V_H}$  the experimental noise level (standard deviation).

**About initial conditions.** It is important to notice that all model parameters are considered in the estimation procedure, including the initial conditions of the model. This is particularly relevant for multistable systems, such as the AFD neuron, which has two stable asymptotic states. For such systems, the convergence to a stable state depends on the initial conditions and a bad initialization choice could result in the inability of the system to fit data. Therefore, by considering  $m_0$  and  $h_0$  as parameters to be estimated, the algorithm can escape from bad regions in the solution space that are due to a bad choice of the initial conditions, and allow the global convergence of the system.

## 2.4 Differential Evolution

Originally proposed by Storn and Price [76], differential evolution (DE) is a simple yet powerful evolutionary algorithm for global optimization, successfully applied in many practical cases [12, 13]. In the context of parameter estimation in conductance-based models (as it is the case in this paper), it has not only been shown to be an effective method [6, 7, 8, 9, 59], but also superior to other optimization methods such as *genetic algorithms*, *simulated annealing* and *particle swarm optimization algorithm* in terms of convergence speed, simulation time, and minimization of the cost function [6, 8].

As every population-based metaheuristic, DE is an optimization method that iteratively optimizes a problem by trying to improve a set of  $NP$  candidate solutions, so-called individuals, that are initially set at random within a given solution space of  $D$  parameters. At each iteration, new individuals (called trial vectors) are constructed by means of two operations: so-called *mutation* and *crossover*. Then *selection* determines which individuals will survive into the next iteration. We define  $x_{i,G}(j)$  as the  $j$ -th parameter of the  $i$ -th individual at generation  $G$ .

In *mutation*, for each target vector  $x_{i,G}$ , a mutant vector  $v_{i,G+1}$  is generated adding a weighted difference between two randomly selected individuals of the generation  $G$  ( $x_{i_2,G}$  and  $x_{i_3,G}$ ) to a third randomly selected one ( $x_{i_1,G}$ ) so that

$$v_{i,G+1} = x_{i_1,G} + F \cdot (x_{i_2,G} - x_{i_3,G}), \quad i_1 \neq i_2 \neq i_3 \neq i \quad (5)$$

where  $F$  is a real constant factor  $\in [0, 2]$  that controls the amplification of the difference vector  $x_{i_2, G} - x_{i_3, G}$ .

In *crossover*, the target vector  $x_{i, G}$  is mixed with the mutated vector  $v_{i, G+1}$  to yield a trial vector  $u_{i, G+1}$  of the form

$$u_{i, G+1} = (u_{i, G+1}(1), u_{i, G+1}(2), \dots, u_{i, G+1}(D))$$

which is generated according to the following scheme:

$$\forall i = 1, \dots, NP, \quad \forall j = 1, \dots, D, \quad u_{i, G+1}(j) = \begin{cases} v_{i, G+1}(j) & \text{if } r < CR \\ x_{i, G}(j) & \text{otherwise} \end{cases} \quad (6)$$

where  $CR \in [0, 1]$  and  $r$  is generated according to a uniform distribution  $\mathcal{U}(0, 1)$ .

Finally, in order to obtain a new generation of individuals, a greedy *selection* is carried out:

$$\forall i = 1, \dots, NP, \quad x_{i, G+1} = \begin{cases} u_{i, G+1} & \text{if } f(u_{i, G+1}) \leq f(x_{i, G}) \\ x_{i, G} & \text{otherwise} \end{cases}$$

where  $f$  is the objective function.

Every individual of the population has to serve once as target vector, so that there are  $NP$  competitions in one generation and the population size is kept constant at  $NP$  with  $NP \geq 4$ . During the mutation operation, if a component of a mutant vector falls out of the bounds of the feasible region (depicted in Table 1), we set this component to the closest boundary value. This approach is particularly efficient if the optimum lies near bounds and produces feasible solutions by making as few alterations to the mutant vector as possible; unlike other techniques consisting in random reinitialization or penalty [64].

Parameters	Minimum value	Maximum Value
$gCa, gKir, gK, gL$	$0nS$	$50nS$
$E_{Ca}$	20mV	150mV
$E_K$	-100mV	0mV
$E_L$	-80mV	30mV
$V_{1/2}^m, V_{1/2}^h, V_{1/2}^{Kir}$	-90mV	0mV
$k_m$	0mV	30mV
$k_h, k_{Kir}$	-30mV	0mV
$\tau_m, \tau_h$	0ds	15ds
$x_m^0, x_h^0$	0	1
$C$	0	10

Table 1: Parameter bounds, determined to be biologically relevant [36, 51, 59].

## 2.5 Differential Evolution for Multi-objective Optimization

In single-objective problems, a solution is better or worse than another solution if its cost function is lower or higher. This is not the case in multi-objective optimization. The notions of *better* and *worse* are replaced by the one of *domination*. A solution  $\theta_1$  dominates another solution  $\theta_2$  if none of its objective values is higher and at least one is lower. Let  $f_1, \dots, f_M$  be the objectives to optimize. In a mathematical sense,  $\theta_1$  dominates  $\theta_2$  if both the following conditions hold:

$$\begin{cases} \forall j \in \{1, \dots, M\}, f_j(\theta_1) \leq f_j(\theta_2) \\ \exists k \in \{1, \dots, M\}, f_k(\theta_1) < f_k(\theta_2) \end{cases} \quad (7)$$

There exist numerous variants of DE for solving multi-objective optimization problems [1, 53, 82, 69, 65, 2, 70]. We select the so-called DEMO (*Differential Evolution for Multi-objective Optimization.*) [69] because it provides a good trade-off between a simplicity of implementation and very good results on benchmarks compared to several state-of-the-art methods in terms of convergence and diversity in obtained solutions [69, 71]. It combines the basic mutation and crossover operators (5) and (6) of the DE for generating new candidates solutions, with the concepts of nondominated front sorting and crowding distance metric derived from NSGA-II [17]. The replacement mechanism in DEMO works as follows:

- the candidate replaces the parent if it dominates it,
- if the parent dominates the candidate, the candidate is discarded,
- otherwise (when the candidate and parent are nondominated with regard to each other), the candidate is added to the population.

After that, if the population size exceed  $NP$ , noted  $Q$ , it needs to be truncated using nondominated sorting and crowding distance metric.

Nondominated sorting is a procedure to classify the exceeding population  $Q$  in different nondominated fronts  $\mathcal{F}_i$ ,  $i = 1, 2, \dots$ , etc. In other words, the solutions of a front  $\mathcal{F}_i$  are not dominated by any member belonging to higher fronts  $\mathcal{F}_j$  where  $j > i$ . In this way, the solutions belonging to the best front  $\mathcal{F}_1$  are those that are not dominated by any member of  $Q$ ; the second front  $\mathcal{F}_2$  are the solutions that are not dominated by any member of the fronts  $\mathcal{F}_j$  for all  $j > 2$ , etc.

Then, the new generation is filled with the best non-dominated front and continues with solutions of the second non-dominated front, followed by the third one, and so on. Since  $|Q| > NP$ , not all fronts may be accommodated in the new generation. When the last acceptable front that cannot be fully accommodated in the population is being considered, instead of arbitrarily discarding some members, we select the solutions which will induce the highest diversity. This procedure allows to promote the diversity in the population. To do so, we assign a crowding distance  $d_i$  to each member  $i$  of the last acceptable front. It is a measure of the normalized search space around  $i$  which is not occupied by any other solution in the population. A solution with a smaller value of the distance is, in a sense, more crowded by other solutions. Therefore, solutions with the highest crowding distance are selected in order to finish to fill the new generation.

## 3 Results

### 3.1 The steady-state current determines the bifurcation structure of non-spiking neurons

In typical voltage-clamp experiments, the membrane potential is stabilized at several values  $V_H$  ( $H$  stands for *hold*) for which the resulting currents are measured. Asymptotic values ( $t \rightarrow \infty$ ) of those currents, depending only on  $V_H$ , are called steady-state currents and noted  $I_\infty(V_H)$ . Mathematically, the steady-state current  $I_\infty$  is the total current  $\sum_{ion} I_{ion}$  flowing across the cell membrane when gating variables  $m$  and  $h$  are at their equilibrium, *i.e.*  $x = x_\infty$  where  $x \in \{m, h\}$ . Therefore, its analytical expression is defined as follows:

$$I_\infty(V) = \sum_{ion} I_{ion\infty}(V) \quad (8)$$

where

$$I_{ion\infty}(V) = g_{ion} m_{ion\infty}^a(V) h_{ion\infty}^b(V) (V - E_{ion})$$

In non-spiking CBMs, we show that the curve  $V \rightarrow I_\infty(V)$  defined in (8) plays a pivotal role in the system dynamics by determining: (i) the number of equilibria as well as their values, and (ii)

all the bifurcations of the resting state along with the values of  $I$  to which they occur. Indeed, any stationary point of gating variables  $x \in \{m, h\}$  must satisfy  $x_* = x_\infty(V_*)$ . Replacing this into the first equation on  $V$ , fixed points  $V_*$  of such models are those that satisfy the equation

$$I_\infty(V_*) = I. \quad (9)$$

In other words, equilibria  $V_*$  correspond to the intersections between the steady-state curve  $I_\infty$  and a horizontal line  $I = c$  where  $c$  is a constant. There are two standard shape of the steady-state curve  $I_\infty$ , monotonic and cubic (Figure 2), each involving fundamentally different neuro-computational properties for non-spiking neurons :

- As shown in Figure 2.A, CBMs with a monotonic steady-state current only have one equilibrium for any value of  $I$ . Non-spiking neurons with such a steady-state current display a near-linear behavior characterized by smoothly depolarization or hyperpolarization from the resting potential, such as the RIM and AIY neurons (Figure 1.A).
- As shown in Figure 2.B, a N-shape curve leads to a saddle-node bifurcation. When  $I = c_1$ , there are 3 equilibria, noted  $V_{1*}^{c_1}$ ,  $V_{2*}^{c_1}$  and  $V_{3*}^{c_1}$ . Increasing  $I$  results in coalescence of two equilibria (the stable  $V_{1*}^{c_1}$  with the unstable  $V_{2*}^{c_1}$ ). The value  $I = c_2$ , at which the equilibria coalesce, is called the *bifurcation value*. For this value of  $I$ , there exist 2 equilibria. For  $I > c_2$ , for example  $I = c_3$ , the system has only one equilibrium. In summary, when the parameter  $I$  increases, a stable and an unstable equilibrium approach, coalesce, and then annihilate each other. Non-spiking neurons with a N-shape steady-state current display a bistable behavior characterized by a voltage jump between the resting potential and a depolarized potential of higher voltage, such as the AFD neuron (Figure 1.B).

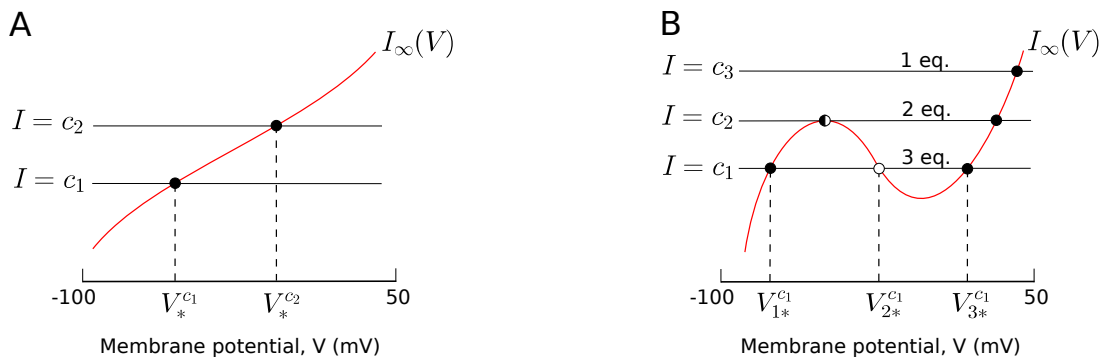


Figure 2: Two typical shapes of the steady-state current  $V \rightarrow I_\infty(V)$ , in red. Intersections of  $I_\infty$  and horizontal line  $I = c$  (with  $c$  constant) correspond to equilibria of the system. We denote stable equilibria as filled circles ●, unstable equilibria as open circles ○ and saddle-node equilibria as ◐. **(A)** Monotonic steady-state current.  $V_*^{c_1}$  and  $V_*^{c_2}$  correspond to equilibria for a current injection  $I = c_1$  and  $I = c_2$  respectively. **(B)** N-shape steady-state current. The number of equilibria of the system depends on the value of  $I$ . For the sake of readability, we highlight equilibria only for  $I = c_1$ , noted  $V_{1*}^{c_1}$ ,  $V_{2*}^{c_1}$  and  $V_{3*}^{c_1}$ .

As a consequence, it can be stated that the steady-state current determines: (i) the bifurcation structure of non-spiking neurons when  $I$  is considered as the bifurcation parameter, and (ii) the equilibrium values of their graded responses to a particular stimuli.

### 3.2 Single-objective optimization may fail to determine a model with generalization capabilities

Single-objective optimization experiments were conducted using stimuli from -15pA and increasing to 25pA by 5pA increments, for the RIM, AIY and AFD neurons. The obtained parameter

values for the three neurons are shown in Appendix B. The generalization capability is then assessed from the voltage trace relative to 30pA and 35pA.

**The bistable AFD neuron.** Figure 3 shows the results obtained for the AFD neuron using the single-objective approach. The high quality of the fitting, which takes into account current injections in the interval  $[-15\text{pA}; 25\text{pA}]$ , can be observed in Figure 3.A. Nonetheless, when considering the resulting steady-state currents of the model in Figure 3.B, it can be observed that the model deteriorates for values higher than 25pA, involving a non-physiological dramatic change in the neuronal dynamics. Figure 3.C confirms this non-physiological response in the evolution of the membrane potential for the 30pA and 35pA traces that are not taken into account during the parameter estimation phase. In fact, as the steady-state current displays a second aberrant and unexpected N-shape for  $I > 25$ , another saddle-node bifurcation occurs at  $I \approx 28.4$  (see Figure 3.D), explaining the drastic rise of the membrane potential trajectory to a new stable state of higher voltage. Thus, it can be concluded that the model fails to predict neuron responses to stimuli not encountered during the parameter estimation process, making it not acceptable and inadequate for the description of the AFD neuron behavior.

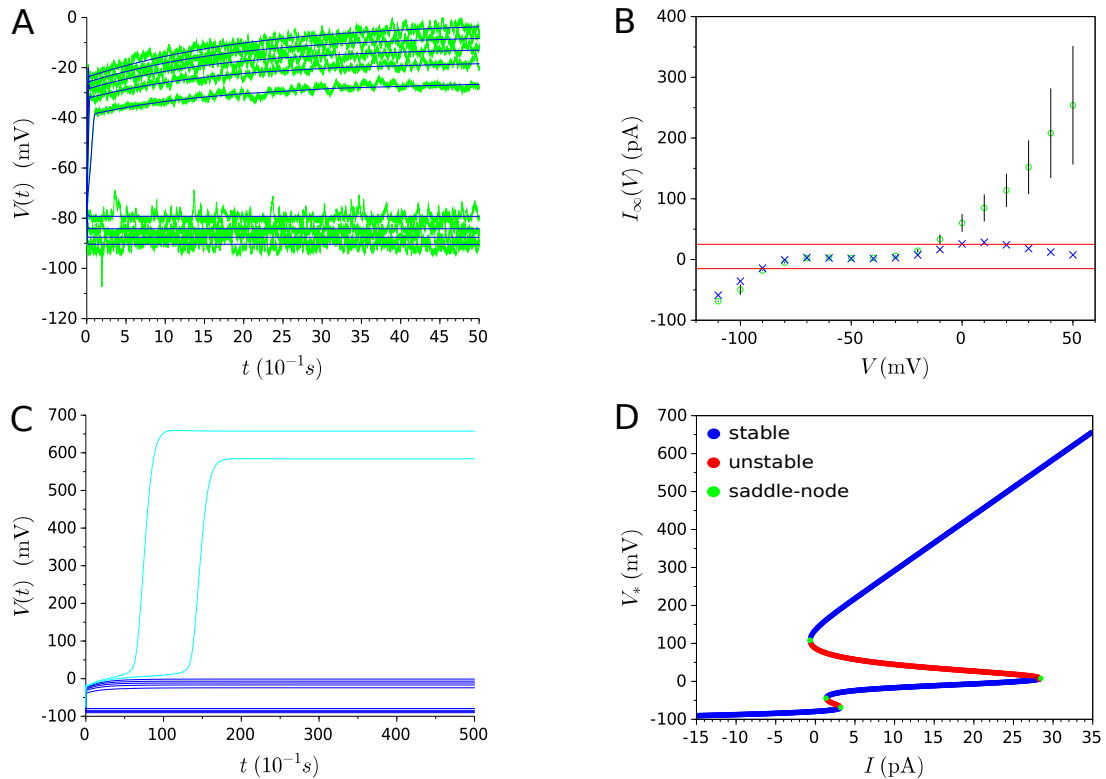


Figure 3: Results of single-objective optimization (evolution of AFD membrane potential): **(A)** Experimental data (represented in green) and  $I_{Ca,p} + I_{Kir} + I_{K,t} + I_L$ -model (represented in blue) overlap for a series of current injection starting from -15pA and increasing to 25pA by 5pA increments. **(B)** Experimental steady-state currents (represented by green circles) and estimated steady-state currents (represented by blue crosses) resulting from the fitting of membrane potential evolution in (A). Red lines delineate the interval  $[-15\text{pA}; 25\text{pA}]$ . **(C)** Dark blue curves represent the evolution of membrane potential for the same values of current injection than in (A) (*i.e.* stimuli starting from -15pA and increasing to 25pA by 5pA increments), whereas light blue ones represent the drastic non-physiological change of voltage traces for novel stimuli (30pA and 35pA). Note the difference of scale regarding y-axis between (A) and (C). **(D)** Bifurcation diagram. Four saddle-node bifurcations occur at  $I \approx -0.66$ ,  $I \approx 1.36$ ,  $I \approx 3.19$  and  $I \approx 28.4$ .

**The near-linear RIM neuron.** As in the case of AFD, Figure 4.A illustrates that the model fits well with experimental data for all series of current injections considered during the optimization process (*i.e.* traces relative to stimuli from -15pA to 25pA by 5pA increments). Additionally, Figure 4.B reveals that the steady-state current does not heavily deteriorate for stimuli higher than 25pA, so that the model should obtain relative good predictive capabilities for new stimuli. This fact is confirmed by Figure 4.C which shows a good fitting for the validation traces (depicted in light blue). Nonetheless, if we analyze the steady-state current in the interval  $I \in [-2\text{pA}; 8\text{pA}]$  (*i.e.* space between the two red lines in Figure 4.B), we can observe a deterioration of the steady-state current shape: instead of a monotonic shape, two N-shape appear. As a consequence, two saddle-node bifurcations occur so that the membrane potential of the model does not display a near-linear behavior as expected, but various jumps arise (as illustrated in Figure 4.D) making the model inadequate for the description of the RIM neuron behavior.

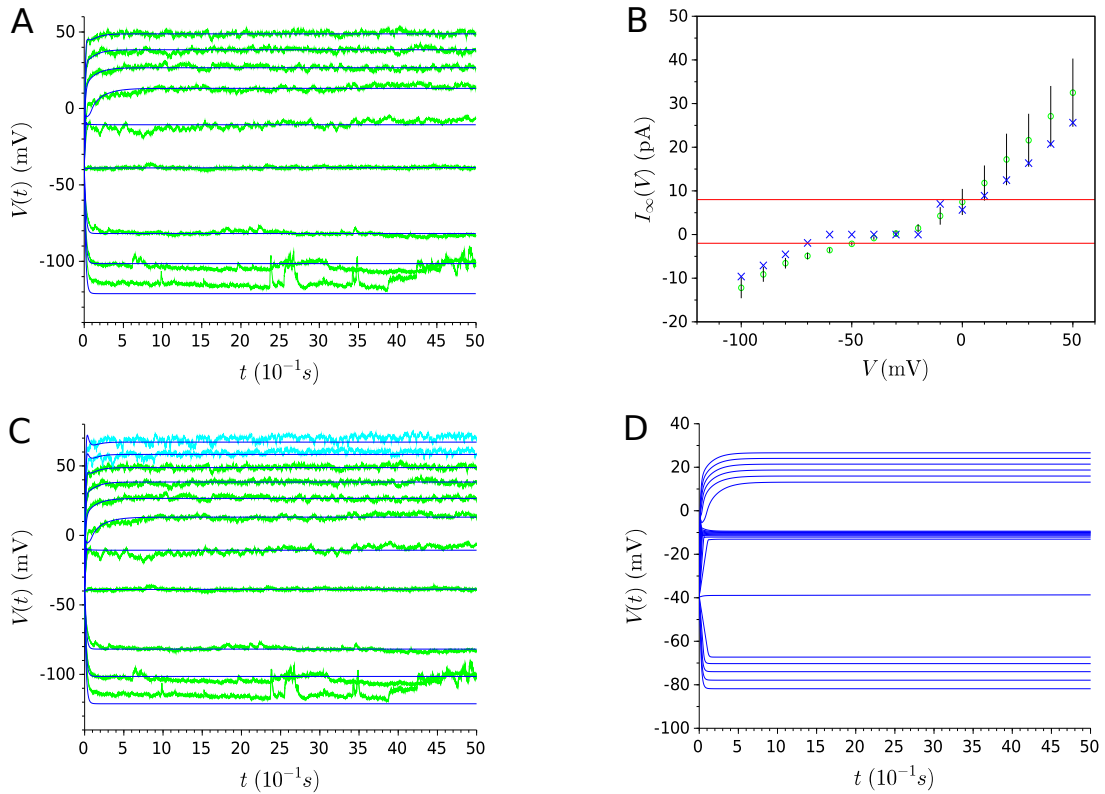


Figure 4: Results of single-objective optimization (evolution of RIM membrane potential): **(A)** Experimental data (represented in green) and  $I_{Ca,p} + I_{Kir} + I_{K,t} + I_L$ -model (represented in blue) overlap for a series of current injection starting from -15pA and increasing to 25pA by 5pA increments. **(B)** Experimental steady-state currents (represented by green circles) and estimated steady-state currents (represented by blue crosses) resulting from the fitting of membrane potential evolution in (A). Red lines delineate the interval  $[-2\text{pA}; 8\text{pA}]$  in which the steady-state current deteriorates. **(C)** Dark blue curves represent the model traces relative to stimuli from -15pA to 25pA by 5pA increments, whereas light blue experimental traces represent experimental traces relative to 30pA and 35pA. **(D)** Evolution of membrane potential for a series of current injection starting from -5pA and increasing to 15pA by 1pA increments. Numerous voltage jumps occur due to the two N-shape of the steady-current displayed in (B) between the red lines.

**The near-linear AIY neuron.** As can be seen in Figure 5.A, the model is capable of predicting accurate responses for traces relative to 30pA and 35pA. However, one can observe a relatively high deterioration of the steady-state current for stimuli higher than 35pA (Figure 5.B). One can then hypothesize that the model may not describe adequately the voltage responses for these stimuli.

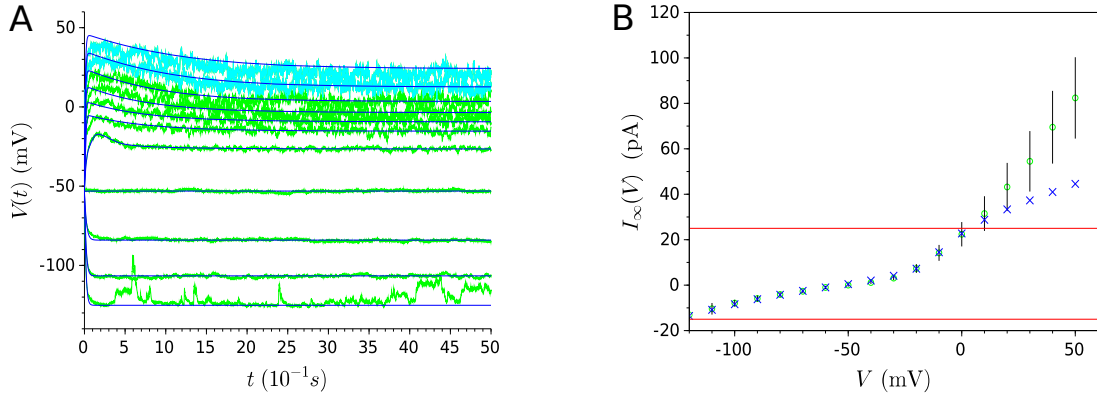


Figure 5: Results of single-objective optimization (evolution of AIY membrane potential): **(A)** Experimental voltages for stimuli starting from -15pA and increasing to 35pA by 5pA increments are represented in green. Estimated voltages resulting from the  $I_{Ca,t} + I_{Kir} + I_{K,p} + I_L$ -model for stimuli going from -15pA to 25pA are represented in dark blue, whereas those relative to 30pA and 35pA are represented in light blue. **(B)** Experimental steady-state currents (represented by green circles) and estimated steady-state currents (represented by blue crosses) resulting from the fitting of membrane potential evolution in (A). Red lines delineate the interval [-15pA;25pA].

### 3.3 A new multi-objective approach suited for determining non-spiking models with generalization capabilities

The previous section shows the importance of capturing the steady-state current in order to get the right underlying bifurcation structure of neurons to predict reasonable neuronal responses. Therefore, in addition to fitting the membrane potential evolution, we should also consider the steady-state current as an additional objective to be fitted to capture the bifurcation dynamics of neurons. Due to the different nature of their respective experimental data, obtained from different experimental procedures with their own intrinsic and extrinsic sources of experimental noise, the voltage and the steady-state current objectives can be conflicting. This conflicting nature imposes a multi-objective treatment of the problem since, under two or more conflicting objectives, there is not a single optimal solution that can optimize all objectives simultaneously. A differential evolution approach adapted for solving multi-objective problems, called DEMO (*Differential Evolution for Multi-objective Optimization*) [69], is used in this paper (see Section 2.5).

Using DEMO as baseline algorithm, the proposed multi-objective approach has been tailored to best suit the nature of the problem, where the primary objective (membrane potential) must prevail over the secondary one (steady-state current). In other words, the primary objective must be favored as it is the one that guarantees quality in the neuronal response while the secondary objective is aimed at capturing the bifurcation structure of the neuron model as to improve its generalization capabilities. We denote the proposed approach DEMO/rand/best/biased.

Inspired by multi-objective guided search [79], the DEMO/rand/best/biased variant tries to guide the search towards an optimal region on the primary objective. To that end, in a preliminary step, a standalone single-objective DE is executed to yield a good candidate solution on the primary objective. This solution is then used to bias the multi-objective approach by integrating it into the initial randomly generated population. In order to reinforce this bias, the

algorithm incorporates a rand/best strategy [24] that greedily uses the best individual on the primary objective to form the trial vector. The aim of this variant is therefore to concentrate and explore the Pareto front region around the best found primary objective solution. The consequence is that the algorithm provides a set of solutions that reproduce the evolution of the membrane potential with high fidelity due to the bias, while taking into account the bifurcation structure of the neuron guided by the secondary objective.

**Automated decision-making process.** The result of a multi-objective optimization process is a set of non-dominated solutions which constitute the best found trade-offs between the conflicting objective functions. If the aim is to adopt one of these solutions as a global solution to the problem, a decision-making process need to be put in place in order to discriminate the selected solution under some criteria. In order to automate this process, we propose a four-stage method that automatically selects a solution capable of reproducing adequate neuronal responses to new stimuli.

- **Step 1:** Split the membrane potential dataset into three sets.

**Procedure:** The membrane potential dataset depicted in Figure 1 is split into three sets: the training set, the validation set, and the test set [47]. The training set, from which the model parameters are estimated, is composed of all the traces of membrane potential for the series of current injections going from -15pA to 25pA by 5pA increments and also the steady-state current. The validation set, used to select a solution with a good predictive capability, is composed of the voltage trace relative to 30pA. The test set, composed of the voltage trace relative to 35pA, is used to assess the model performance from data not used in any part of the learning or decision-making process. The different sets are summarized in Table 2.

Training set	Validation set	Test set
<ul style="list-style-type: none"> <li>• Voltage traces for stimuli going from -15pA to 25pA.</li> <li>• Steady-state current.</li> </ul>	<ul style="list-style-type: none"> <li>• Voltage trace relative to 30pA.</li> </ul>	<ul style="list-style-type: none"> <li>• Voltage trace relative to 35pA.</li> </ul>

Table 2: Training, validation and test sets.

- **Step 2:** Determining the set of non-dominated solutions.

**Procedure:** 10 runs with different random seeds of the multi-objective optimization approach DEMO/rand/best/biased are conducted using the training set. The final set of solutions (that we denote as  $S$ ) is composed of all non-dominated solutions found during these independent runs.

**Input:** 6000 solutions (600 solutions per run  $\times$  10 independent runs).

**Output:** A set  $S$  composed of all non-dominated solutions.

- **Step 3:** Selecting solutions with a correct bifurcation structure.

**Procedure:** This step aims at eliminating from the set  $S$  the solutions that do not display the right expected shape of the steady-state current  $I_\infty$ , *i.e.* monotonic for the near-linear neurons, and N-shape for the bistable ones. To do so, we first compute the first-order derivative of  $I_\infty$ , noted  $I'_\infty$ . For the near-linear neurons, we then verify that  $I'_\infty(V) > 0$  for any values of  $V \in [-100\text{mV}; 50\text{mV}]$  to ensure the monotonicity of  $I_\infty$ . For the bistable neurons,  $I'_\infty$  has to be positive, then negative, and positive again to ensure the N-shape of  $I_\infty$ . These are the conditions we verify to select solutions with a correct bifurcation structure.

**Input:** The set  $S$  composed of all non-dominated solutions.

**Output:** A set  $S_1$  composed of all non-dominated solutions displaying appropriate bifurcation structure.

- **Step 4:** Selecting the best solution according to the validation trace.

**Procedure:** Using equation (3), compute the numerical scores of all solutions in  $S_1$  by only considering the validation trace. The solution with the lowest score, *i.e.* minimal cost function, is the one selected.

**Input:** The set  $S_1$  composed of non-dominated solutions displaying appropriate bifurcation structure.

**Output:** The final selected solution.

The proposed decision-making process does not take into account the test trace. The aim is to reserve a trace that has not been used in any part of the learning or decision-making process to assess the quality of the solution found. In the next section, we show that our proposed approach proves to be effective.

### 3.4 Obtaining non-spiking conductance-based models with generalization capabilities

In order to obtain a model with generalization capabilities, we follow the approach developed in the previous section. The DEMO/rand/best/biased algorithm is run with different values of control parameters  $NP$ ,  $F$  and  $CR$  in order to fine-tune its search capabilities. The values that we recommend are  $NP = 600$ ,  $F = 1.5$  and  $CR = 0.3$  with a number of 2000 iterations. For the three neurons, the model parameters obtained from the automated decision-making process described in the previous section are displayed in Appendix B.

**Generalization capability of models.** For each neuron under study, it can be observed in Figure 6.A that the curves of the models fit well with experimental data in all series of current injections, including the test trace not used in any part of the model learning. The quality of the fitting is maintained throughout the entire evolution of the membrane potential. Furthermore, the steady-state current shape (Figure 6.B), which determines the underlying bifurcation structure of non-spiking neurons, is captured for all neurons: a monotonic steady-state current for the RIM and AIY neurons, and a N-shape one for AFD. In this way, we constrain the RIM and AIY models to a near-linear behavior, and the AFD neuron to a bistable one, even in response to novel different stimuli not used during the model’s building. In the light of these results, it can be concluded that the proposed approach allows to get models with good generalization capabilities.

**The steady-state current objective requires a relatively small deterioration to get models with predictive capabilities.** Both objectives cannot be simultaneously optimized due to their conflicting nature. On the one hand, the steady-state curve for each neuron is obtained from the average of several different cells, while the membrane potentials are representative recordings from a single cell without averaging. On the other hand, the steady-state current and the voltage data are obtained from different experimental procedures with their own intrinsic and extrinsic sources of experimental noise [22, 55, 18, 27]. Therefore, obtaining a perfect fitting of both objectives simultaneously is not feasible. Furthermore, the relative deterioration of the fitting for high steady-state currents in Figure 6.B is correlated with higher values of the standard deviation at this level. Actually, these deteriorations are necessary to obtain models able to characterize voltage behavior. Indeed, as shown in Figure 7, a model that perfectly fits the steady-state current (Figure 7.A) does not accurately reproduce the given voltage traces and fails to get the predictive capability (Figure 7.B).

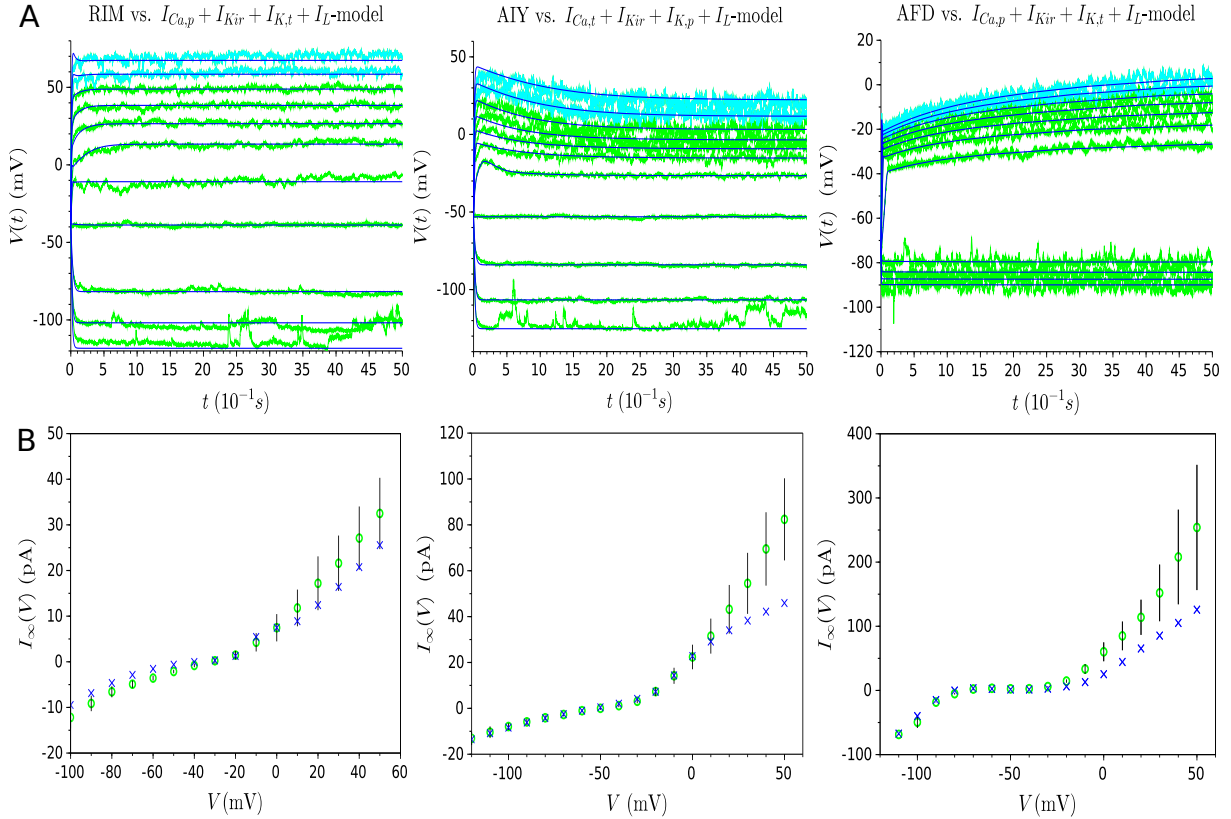


Figure 6: Results of multi-objective optimization for the RIM, AIY and AFD neurons. **(A)** Green traces represent the experimental membrane potential evolution for a series of current injections, in spans of 5 seconds, starting from -15pA and increasing to 25pA by 5pA increments. The light blue traces represent the validation and test set (*i.e.* traces relative to 30pA and 35pA). The dark blue traces represent the respective model for each neuron. **(B)** Experimental steady-state currents (represented by green circles) and estimated steady-state currents (represented by blue crosses) resulting from the multi-objectif optimization.

## 4 Discussion

The proposed method, based on theoretical mathematical development and experimental validation, provides a systematic approach to build non-spiking models with generalization capabilities. In this section, we discuss both the biological and modeling implications of this methodology.

**Implications on the modeling of non-spiking neurons in general.** In this paper, our proposed approach was applied on various non-spiking *C. elegans* neurons, representative of the behavior of known types of non-spiking neurons (near-linear and bistable). Such neurons are not specific to *C. elegans* so that the proposed method, based on general analysis of the bifurcation structure of non-spiking neurons, is expected to be successfully applied more broadly to different non-spiking neuronal cell types. Indeed, as stated in the introduction, this type of neurons are ubiquitous in a large variety of nervous tissues in both vertebrates and invertebrates species, *e.g.* in the human retina neurons [25], numerous interneurons in insects and crustaceans [68], the motoneurons of the *Ascaris* worm [14, 15], or most of the *C. elegans* neurons [28]. They have been found in sensorimotor and central pattern generator circuits, proved to be central in neuronal integration [68] and to provide a determining mechanism for the control of motor behavior [10, 46, 45].

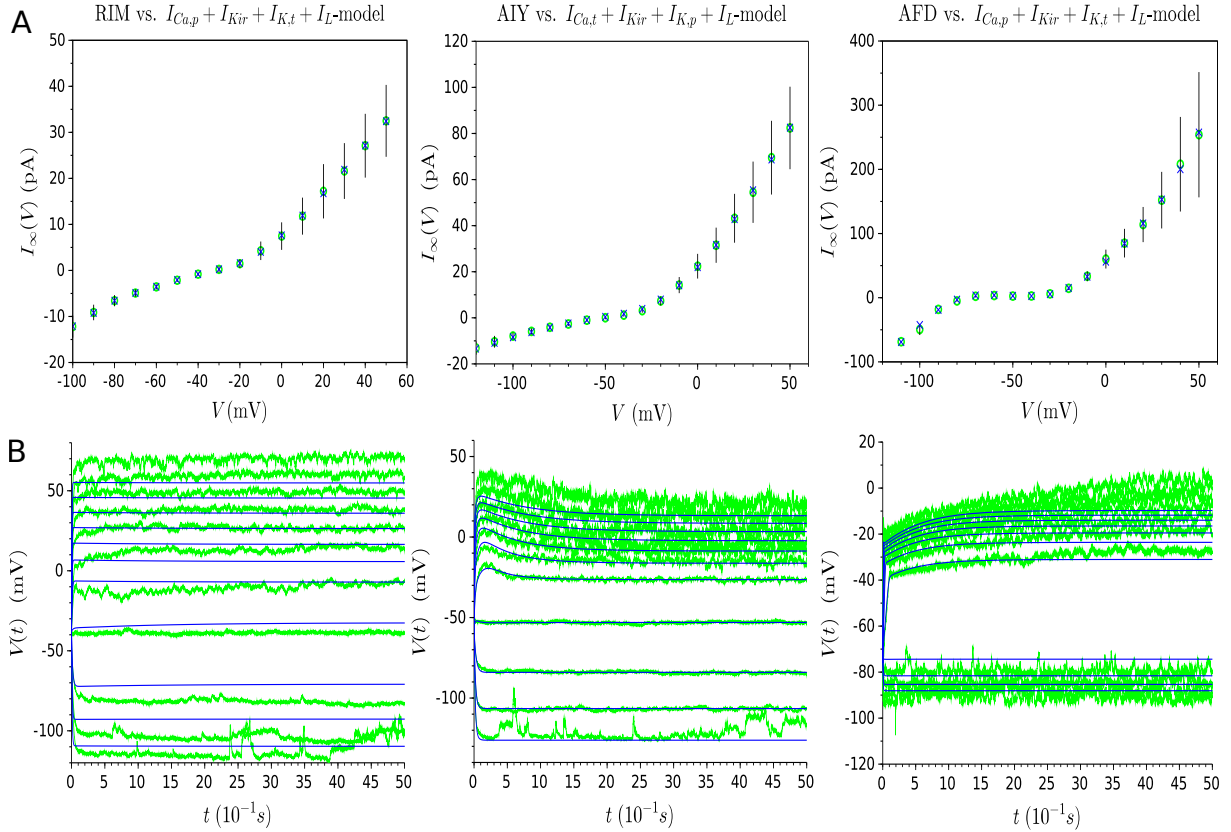


Figure 7: Solutions obtained from multi-objective optimization with perfect fitting of the steady-state current. **(A)** Experimental steady-state currents (represented by green circles) and estimated steady-state currents (represented by blue crosses) resulting from the multi-objective optimization. **(B)** Green (resp. blue) traces represent the experimental (resp. estimated) membrane potential evolution for a series of current injections, in spans of 5 seconds, starting from -15pA and increasing to 35pA by 5pA increments. Solutions with a perfect fitting of the steady-state current fail to describe the behavior voltage of neurons, showing that its deterioration is necessary to get adequate models.

**Implications on the modeling of the *C. elegans*' neuronal diversity.** Numerous recordings of *C. elegans*' neuronal activity have already been performed [28, 60, 23, 67, 58, 48, 26, 49, 50, 51, 19]. Liu *et al.* [51] classify the recorded neurons into four large distinct classes based on the features of the I-V curve (Figure 1). This classification is described in detail in Table 3. Among the different classes, the authors enumerate three types of non-spiking neurons, of which RIM, AIY and AFD are representative examples, and a fourth type involving the spiking neuron AWA. However, the electrophysiological properties of many *C. elegans* neurons are unknown yet, suggesting that additional types of neurons could be discovered in the future. The results presented in this paper show that the proposed method is capable of capturing the behavior of the current non-spiking neuronal diversity of *C. elegans* and could be successfully applied to model new non-spiking neurons.

**Implications on the modeling of the *C. elegans*' nervous system.** Due to its fully mapped connectome and its small number of neurons, the *C. elegans* nervous system is the ideal candidate to be modeled in order to investigate how behavior emerges from its underlying physiological processes [78, 74, 37]. Modeling the nervous system of *C. elegans* involves two fundamental stages [38]: one relative to the modeling of the neuronal connectivity (connectome) and the other relative to the modeling of the neuronal dynamic. Nowadays, the vast majority of

Neuron classes	Class 1	Class 2	Class 3
Inward current features	Near-zero inward currents under hyperpolarizations.	Near-zero inward currents under hyperpolarizations.	Large sustained inwardly currents under hyperpolarizations.
Outward current features	Rapid inactivating outward currents under depolarizations : lack of large sustained currents.	Non-inactivating outward currents under depolarizations.	Large inactivating outward currents under depolarizations.
Neurons	<b>RIM</b> [51] AVA [48, 50, 58] PLM [60] AVE [48]	<b>AIY</b> [51, 23] VA5 [49, 50] VB6 [49, 50]	<b>AFD</b> [51, 67] ASER [28] RMD [58] AWC [67] ASH [26] AIA [19]

Table 3: Classification of the three types of non-spiking neurons in *C. elegans*, according to their current-voltage relationships. RIM, AIY and AFD neurons are representatives of the class 1, 2 and 3 respectively.

modeling works on *C. elegans* nervous system employ the well-established connectome but they do not take into account the specificities of the neuronal dynamics [80, 72, 66, 42, 63, 43, 11, 61, 38, 44, 54]. Indeed, these works rather consider: (i) a homogeneous model for each neuron of the network (while *C. elegans* neurons display a large repertoire of behaviors), and (ii) a neuron model that do not correspond to the behavior of *C. elegans* neurons. The discordance between the accuracy of the connectome and the inaccuracy of the neuronal dynamic considered is explained by the lack of biophysical information for most neurons, making the building of conductance-based model adapted to *C. elegans*' neuronal dynamic currently challenging [74]. As pointed out by Sarma *et al.* [74], building such neuron models is a key remaining component to make *C. elegans* nervous system modeling studies adequate for biological research.

In particular, we would like to emphasize an open problem where computational works could play an important role in order to fully understand the flow of information within the nematode's nervous system [4]. If one wants to deepen further our understanding of the *C. elegans* nervous system, it is of paramount importance to gather information about what most of the neurons' connections do, their intrinsic nature (excitatory or inhibitory), and the strengths of such connections [4]. Actually, the connectome does not unveil such information [41]. To address that issue, some computational studies [80, 66, 63, 11, 61, 44] adopt an evolutionary approach in which the algorithm determines both the strength and nature of connections in order to obtain observable, realistic worm behavior. In such studies, the functional circuits studied are made up of homogeneous neuron models irrelevant to characterize the heterogeneity of *C. elegans* neurons and to represent acceptably their behavior (*e.g.* the homogeneous Izhikevich spiking model [35] is considered in [63] and [11], or the Hindmarsh-Rose spiking model in [44]). Therefore, even if the macroscopic behavior of *C. elegans* is accurately reproduced, the results on the strength and nature of neuron connections may not be biologically adequate. We argue that the current paper provides a systematic approach and method to build conductance-based models capturing the dynamic of non-spiking *C. elegans*' neurons, so that the second stage relative to the *C. elegans* neuronal dynamic modeling can be fulfilled.

**Implications on multicompartmental conductance-based modeling.** It is worth noting that characterizing a neuron as “spiking” or “non-spiking” is only relative to the site of recording. The fact that a neuron is spiking in one part does not exclude that it may have non-spiking activity in other parts, such as in the dendrites. Indeed, even in spiking neurons, the integrative life of the cell is *predominantly* performed through graded electrical activity via the dendrites [68, 52]. The complex geometry of the dendritic tree, combined with its active and passive membrane properties, play a key role in the way neurons integrate synaptic inputs. Therefore, dendrites strongly influence both the timing and probability of neuronal output [77, 62]. In order to take into account the heterogeneity of the dendritic morphology as well as the different electrical characteristics between the regions (a.k.a. compartments) of the neuron, numerous modeling studies [56, 57, 34] use multicompartmental conductance-based models [16], which allow to develop more realistic and morphologically accurate models. The methodology presented in this paper could be used in a systematic way to gain leverage in the modeling of the non-spiking parts of different neuronal cell types.

## Author contributions

**Conceptualization:** Naudin Loïs, Jiménez Laredo Juan Luis, Corson Nathalie, Liu Qiang

**Data curation:** Naudin Loïs, Liu Qiang

**Formal analysis:** Naudin Loïs, Jiménez Laredo Juan Luis

**Funding acquisition:** Liu Qiang

**Investigation:** Naudin Loïs, Liu Qiang, Jiménez Laredo Juan Luis, Corson Nathalie

**Methodology:** Naudin Loïs, Jiménez Laredo Juan Luis, Corson Nathalie

**Project administration:** Naudin Loïs, Corson Nathalie

**Resources:** Liu Qiang

**Software:** Naudin Loïs

**Supervision:** Corson Nathalie, Jiménez Laredo Juan Luis, Naudin Loïs

**Validation:** Naudin Loïs, Jiménez Laredo Juan Luis, Corson Nathalie, Liu Qiang

**Vizualization:** Naudin Loïs, Liu Qiang

**Writing – original draft:** Naudin Loïs

**Writing – review & editing:** Naudin Loïs, Jiménez Laredo Juan Luis, Corson Nathalie, Liu Qiang

## Data Availability Statement

All code used for running experiments, model fitting, and to produce the results and analyses are available on a GitHub repository at <https://zenodo.org/badge/latestdoi/388104503>.

Raw electrophysiological recording traces shown in this paper have been deposited into Mendeley (<https://doi.org/10.17632/6pgdf3zrp3.1>)

## **Declaration of Interests**

The authors declare no competing interests.

## A Full-fledged material description

$I_{Ca,p} +$ $I_{Kir} +$ $I_{K,t} + I_{L-}$ model	$\begin{cases} C\dot{V} = -g_{Ca}m_{Ca}(V - E_{Ca}) - g_{Kir}h_{Kir\infty}(V)(V - E_K) - g_Km_Kh_K(V - E_K) - g_L(V - E_L) + I \\ m_{Ca} = \frac{m_{Ca\infty}(V) - m_{Ca}}{\tau_{m_{Ca}}}, \quad m_{Ca\infty}(V) = \left(1 + \exp\left(\frac{V^{m_{Ca}} - V}{k_{m_{Ca}}}\right)\right)^{-1} \\ m_K = \frac{m_{K\infty}(V) - m_K}{\tau_{m_K}}, \quad m_{K\infty}(V) = \left(1 + \exp\left(\frac{V^{m_K} - V}{k_{m_K}}\right)\right)^{-1} \\ h_K = \frac{h_{K\infty}(V) - h_K}{\tau_{h_K}}, \quad h_{K\infty}(V) = \left(1 + \exp\left(\frac{V^{h_K} - V}{k_{h_K}}\right)\right)^{-1} \end{cases}$ $I_\infty(V_H) = g_{Ca}m_{Ca\infty}(V_H)(V_H - E_{Ca}) + g_{Kir}h_{Kir\infty}(V_H)(V_H - E_K) + g_Km_{K\infty}(V_H)h_{K\infty}(V_H)(V_H - E_K) + g_L(V_H - E_L)$ $\theta_V = [g_{Ca} \ g_{Kir} \ g_K \ g_L \ E_{Ca} \ E_K \ E_L \ V_{1/2}^{m_{Ca}} \ V_{1/2}^{Kir} \ V_{1/2}^{m_K} \ V_{1/2}^{h_K} \ k_{m_{Ca}} \ k_{Kir} \ k_{m_K} \ k_{h_K} \ \tau_{m_{Ca}} \ \tau_{m_K} \ \tau_{h_K} \ m_{Ca}^0 \ m_K^0 \ h_K^0 \ C]$ $\theta_{SS} = [g_{Ca} \ g_{Kir} \ g_K \ g_L \ E_{Ca} \ E_K \ E_L \ V_{1/2}^{m_{Ca}} \ V_{1/2}^{Kir} \ V_{1/2}^{m_K} \ V_{1/2}^{h_K} \ k_{m_{Ca}} \ k_{Kir} \ k_{m_K} \ k_{h_K}]$
$I_{Ca,t} +$ $I_{Kir} +$ $I_{K,p} + I_{L-}$ model	$\begin{cases} C\dot{V} = -g_{Ca}m_{Ca}h_{Ca}(V - E_{Ca}) - g_{Kir}h_{Kir\infty}(V)(V - E_K) - g_Km_K(V - E_K) - g_L(V - E_L) + I \\ m_{Ca} = \frac{m_{Ca\infty}(V) - m_{Ca}}{\tau_{m_{Ca}}}, \quad m_{Ca\infty}(V) = \left(1 + \exp\left(\frac{V^{m_{Ca}} - V}{k_{m_{Ca}}}\right)\right)^{-1} \\ h_{Ca} = \frac{h_{Ca\infty}(V) - h_{Ca}}{\tau_{h_{Ca}}}, \quad h_{Ca\infty}(V) = \left(1 + \exp\left(\frac{V^{h_{Ca}} - V}{k_{h_{Ca}}}\right)\right)^{-1} \\ m_K = \frac{m_{K\infty}(V) - m_K}{\tau_{m_K}}, \quad m_{K\infty}(V) = \left(1 + \exp\left(\frac{V^{m_K} - V}{k_{m_K}}\right)\right)^{-1} \end{cases}$ $I_\infty(V_H) = g_{Ca}m_{Ca\infty}(V_H)h_{Ca\infty}(V_H)(V_H - E_{Ca}) + g_{Kir}h_{Kir\infty}(V_H)(V_H - E_K) + g_Km_{K\infty}(V_H)(V_H - E_K) + g_L(V_H - E_L)$ $\theta_V = [g_{Ca} \ g_{Kir} \ g_K \ g_L \ E_{Ca} \ E_K \ E_L \ V_{1/2}^{m_{Ca}} \ V_{1/2}^{h_{Ca}} \ V_{1/2}^{Kir} \ V_{1/2}^{m_K} \ k_{m_{Ca}} \ k_{h_{Ca}} \ k_{Kir} \ k_{m_K} \ \tau_{m_{Ca}} \ \tau_{h_{Ca}} \ \tau_{m_K} \ m_{Ca}^0 \ h_{Ca}^0 \ m_K^0 \ C]$ $\theta_{SS} = [g_{Ca} \ g_{Kir} \ g_K \ g_L \ E_{Ca} \ E_K \ E_L \ V_{1/2}^{m_{Ca}} \ V_{1/2}^{h_{Ca}} \ V_{1/2}^{Kir} \ V_{1/2}^{m_K} \ k_{m_{Ca}} \ k_{h_{Ca}} \ k_{Kir} \ k_{m_K}]$

## B Estimated parameters for each of the models

	Single-objective			Multi-objective		
	RIM	AIY	AFD	RIM	AIY	AFD
$g_{Ca}$	0.68	0.124	0.06	0.68	0.136	2.98
$g_{Kir}$	0.254	0.157	2.02	0.254	0.156	2.37
$g_K$	1.16	0.223	6.05	1.812	0.22	7.36
$g_L$	0.0002	0.14	0.0001	0.0008	0.14	0.0001
$E_{Ca}$	20.16	135.9	146.05	20.59	127.4	20
$E_K$	-62.18	-98.23	-79.3	-38.59	-98.3	-79.74
$E_L$	-37.6	-41.07	-90	-90	-41.1	-90
$V_{1/2}^{m_{Ca}}$	-5.5	-19.09	-22.1	-2	-19.09	-2
$V_{1/2}^{h_{Ca}}$		-21.24			-21.28	
$V_{1/2}^{m_K}$	-9.38	-17.71	-2.83	-9.63	-17.99	-2.83
$V_{1/2}^{h_K}$	-65.7		-46.5	-24.27		-46.56
$V_{1/2}^{h_{Kir}}$	-24.27	-90	-84.16	-86.98	-89.95	-85.74
$k_{m_{Ca}}$	1.6	4.67	8.99	5.19	4.65	8.67
$k_{h_{Ca}}$		-17.62			-16.06	
$k_{m_K}$	1.28	7.39	9.99	4.84	7.41	9.99
$k_{h_K}$	-23.44		-24.21	-21.84		-30
$k_{h_{Kir}}$	-1.32	-30	-8.92	-30	-29.98	-8.92
$\tau_{m_{Ca}}$	0.399	0.0001	19.43	0.548	0.0001	12.96
$\tau_{h_{Ca}}$		10.59			11.12	
$\tau_{m_K}$	0.03	0.0005	0.03	0.05	0.001	0.03
$\tau_{h_K}$	0.61		6.16	0.6		3.71
$m_{Ca}^0$	0.002	0.001	0.002	0.001	0.33	0.001
$h_{Ca}^0$		0.80			0.78	
$m_K^0$	0.643	0.999	0.001	0.001	0.74	0.001
$h_K^0$	0.113		0.67	0.113		0.59
$C$	0.042	0.04	0.058	0.04	0.04	0.058

## References

- [1] Hussein A Abbass, Ruhul Sarker, and Charles Newton. Pde: a pareto-frontier differential evolution approach for multi-objective optimization problems. In *Proceedings of the 2001 Congress on Evolutionary Computation (IEEE Cat. No. 01TH8546)*, volume 2, pages 971–978. IEEE, 2001.
- [2] JA Adeyemo and FAO Otieno. Multi-objective differential evolution algorithm for solving engineering problems. *Journal of Applied Sciences*, 9(20):3652–3661, 2009.
- [3] Aymen Balti, Valentina Lanza, and Moulay Aziz-Alaoui. A multi-base harmonic balance method applied to hodgkin-huxley model. *Mathematical Biosciences & Engineering*, 15(3):807, 2018.
- [4] Cornelia I Bargmann and Eve Marder. From the connectome to brain function. *Nature methods*, 10(6):483, 2013.
- [5] Sydney Brenner. The genetics of caenorhabditis elegans. *Genetics*, 77(1):71–94, 1974.
- [6] Laure Buhry, Sylvain Saïghi, Audrey Giremus, Eric Grivel, and Sylvie Renaud. Parameter estimation of the hodgkin-huxley model using metaheuristics: application to neuromimetic analog integrated circuits. In *2008 IEEE Biomedical Circuits and Systems Conference*, pages 173–176. IEEE, 2008.
- [7] Laure Buhry, Audrey Giremus, Eric Grivel, Sylvain Saïghi, and Sylvie Renaud. New variants of the differential evolution algorithm: application for neuroscientists. In *2009 17th European Signal Processing Conference*, pages 2352–2356. IEEE, 2009.
- [8] Laure Buhry, Filippo Grassia, Audrey Giremus, Eric Grivel, Sylvie Renaud, and Sylvain Saïghi. Automated parameter estimation of the hodgkin-huxley model using the differential evolution algorithm: application to neuromimetic analog integrated circuits. *Neural computation*, 23(10):2599–2625, 2011.
- [9] Laure Buhry, Michele Pace, and Sylvain Saïghi. Global parameter estimation of an hodgkin-huxley formalism using membrane voltage recordings: application to neuro-mimetic analog integrated circuits. *Neurocomputing*, 81:75–85, 2012.
- [10] M Burrows, GJ Laurent, and LH Field. Proprioceptive inputs to nonspiking local interneurons contribute to local reflexes of a locust hindleg. *Journal of Neuroscience*, 8(8):3085–3093, 1988.
- [11] Alicia Costalago-Meruelo, Pedro Machado, Kofi Appiah, Andoni Mujika, Peter Leskovsky, Roberto Alvarez, Gorka Epelde, and T Martin McGinnity. Emulation of chemical stimulus triggered head movement in the c. elegans nematode. *Neurocomputing*, 290:60–73, 2018.
- [12] Swagatam Das and Ponnuthurai Nagaratnam Suganthan. Differential evolution: A survey of the state-of-the-art. *IEEE transactions on evolutionary computation*, 15(1):4–31, 2010.
- [13] Swagatam Das, Sankha Subhra Mullick, and Ponnuthurai N Suganthan. Recent advances in differential evolution—an updated survey. *Swarm and Evolutionary Computation*, 27:1–30, 2016.
- [14] Ralph E Davis and AO Stretton. Signaling properties of ascaris motorneurons: graded active responses, graded synaptic transmission, and tonic transmitter release. *Journal of Neuroscience*, 9(2):415–425, 1989.

- [15] RE Davis and AO Stretton. Passive membrane properties of motorneurons and their role in long-distance signaling in the nematode ascaris. *Journal of Neuroscience*, 9(2):403–414, 1989.
- [16] Peter Dayan and Laurence F Abbott. *Theoretical neuroscience: computational and mathematical modeling of neural systems*. MIT press, 2001.
- [17] Kalyanmoy Deb, Amrit Pratap, Sameer Agarwal, and TAMT Meyarivan. A fast and elitist multiobjective genetic algorithm: Nsga-ii. *IEEE transactions on evolutionary computation*, 6(2):182–197, 2002.
- [18] Alain Destexhe and Michelle Rudolph-Lilith. *Neuronal noise*, volume 8. Springer Science & Business Media, 2012.
- [19] May Dobosiewicz, Qiang Liu, and Cornelia I Bargmann. Reliability of an interneuron response depends on an integrated sensory state. *Elife*, 8:e50566, 2019.
- [20] Shaul Druckmann. Automated parameter constraining of single-neuron models. In *The Computing Dendrite*, pages 465–482. Springer, 2014.
- [21] Shaul Druckmann, Thomas K Berger, Felix Schürmann, Sean Hill, Henry Markram, and Idan Segev. Effective stimuli for constructing reliable neuron models. *PLoS Comput Biol*, 7(8):e1002133, 2011.
- [22] A Aldo Faisal, Luc PJ Selen, and Daniel M Wolpert. Noise in the nervous system. *Nature reviews neuroscience*, 9(4):292–303, 2008.
- [23] Serge Faumont, Thomas Boulin, Oliver Hobert, and Shawn R Lockery. Developmental regulation of whole cell capacitance and membrane current in identified interneurons in *c. elegans*. *Journal of neurophysiology*, 95(6):3665–3673, 2006.
- [24] V. Feoktistov and S. Janaqi. Generalization of the strategies in differential evolution. In *18th International Parallel and Distributed Processing Symposium, 2004. Proceedings.*, 2004.
- [25] Greg D Field and EJ Chichilnisky. Information processing in the primate retina: circuitry and coding. *Annu. Rev. Neurosci.*, 30:1–30, 2007.
- [26] Shana L Geffeney, Juan G Cueva, Dominique A Glauser, Joseph C Doll, Tim Hau-Chen Lee, Misty Montoya, Snetu Karania, Arman M Garakani, Beth L Pruitt, and Miriam B Goodman. Deg/enac but not trp channels are the major mechanoelectrical transduction channels in a *c. elegans* nociceptor. *Neuron*, 71(5):845–857, 2011.
- [27] Wulfram Gerstner, Werner M Kistler, Richard Naud, and Liam Paninski. *Neuronal dynamics: From single neurons to networks and models of cognition*. Cambridge University Press, 2014.
- [28] Miriam B Goodman, David H Hall, Leon Avery, and Shawn R Lockery. Active currents regulate sensitivity and dynamic range in *c. elegans* neurons. *Neuron*, 20(4):763–772, 1998.
- [29] Alan L Hodgkin and Andrew F Huxley. A quantitative description of membrane current and its application to conduction and excitation in nerve. *The Journal of physiology*, 117(4):500–544, 1952.
- [30] Alan L Hodgkin, Andrew F Huxley, and Bernard Katz. Measurement of current-voltage relations in the membrane of the giant axon of loligo. *The Journal of physiology*, 116(4):424–448, 1952.

- [31] Allan L Hodgkin and Andrew F Huxley. Currents carried by sodium and potassium ions through the membrane of the giant axon of loligo. *The Journal of physiology*, 116(4):449–472, 1952.
- [32] Allan L Hodgkin and Andrew F Huxley. The components of membrane conductance in the giant axon of loligo. *The Journal of physiology*, 116(4):473–496, 1952.
- [33] Allan L Hodgkin and Andrew F Huxley. The dual effect of membrane potential on sodium conductance in the giant axon of loligo. *The Journal of physiology*, 116(4):497–506, 1952.
- [34] Elisabetta Iavarone, Jane Yi, Ying Shi, Bas-Jan Zandt, Christian O’reilly, Werner Van Geit, Christian Rössert, Henry Markram, and Sean L Hill. Experimentally-constrained biophysical models of tonic and burst firing modes in thalamocortical neurons. *PLOS Computational Biology*, 15(5):e1006753, 2019.
- [35] Eugene M Izhikevich. Simple model of spiking neurons. *IEEE Transactions on neural networks*, 14(6):1569–1572, 2003.
- [36] Eugene M Izhikevich. *Dynamical systems in neuroscience*. MIT press, 2007.
- [37] Eduardo J Izquierdo. Role of simulation models in understanding the generation of behavior in *c. elegans*. *Current Opinion in Systems Biology*, 13:93–101, 2019.
- [38] Jimin Kim, William Leahy, and Eli Shlizerman. Neural interactome: Interactive simulation of a neuronal system. *Frontiers in Computational Neuroscience*, 13:8, 2019.
- [39] Christof Koch. *Biophysics of computation: information processing in single neurons*. Oxford university press, 1999.
- [40] Kristin Koch, Judith McLean, Ronen Segev, Michael A Freed, Michael J Berry II, Vijay Balasubramanian, and Peter Sterling. How much the eye tells the brain. *Current Biology*, 16(14):1428–1434, 2006.
- [41] Nancy J Kopell, Howard J Gritton, Miles A Whittington, and Mark A Kramer. Beyond the connectome: the dynamome. *Neuron*, 83(6):1319–1328, 2014.
- [42] James Kunert, Eli Shlizerman, and J Nathan Kutz. Low-dimensional functionality of complex network dynamics: Neurosensory integration in the caenorhabditis elegans connectome. *Physical Review E*, 89(5):052805, 2014.
- [43] James M Kunert, Joshua L Proctor, Steven L Brunton, and J Nathan Kutz. Spatiotemporal feedback and network structure drive and encode caenorhabditis elegans locomotion. *PLoS computational biology*, 13(1), 2017.
- [44] Enrico Lanza, Silvia Di Angelantonio, Giorgio Gosti, Giancarlo Ruocco, and Viola Folli. A recurrent neural network model of *c. elegans* responses to aversive stimuli. *Neurocomputing*, 430:1–13, 2021.
- [45] G Laurent and M Burrows. Intersegmental interneurons can control the gain of reflexes in adjacent segments of the locust by their action on nonspiking local interneurons. *Journal of Neuroscience*, 9(9):3030–3039, 1989.
- [46] Gilles Laurent and Malcolm Burrows. Distribution of intersegmental inputs to nonspiking local interneurons and motor neurons in the locust. *Journal of Neuroscience*, 9(9):3019–3029, 1989.
- [47] Yann Le Cun. *Quand la machine apprend: la révolution des neurones artificiels et de l’apprentissage profond*. Odile Jacob, 2019.

- [48] Theodore H Lindsay, Tod R Thiele, and Shawn R Lockery. Optogenetic analysis of synaptic transmission in the central nervous system of the nematode *caenorhabditis elegans*. *Nature communications*, 2:306, 2011.
- [49] Ping Liu, Bojun Chen, and Zhao-Wen Wang. Slo-2 potassium channel is an important regulator of neurotransmitter release in *caenorhabditis elegans*. *Nature communications*, 5: 5155, 2014.
- [50] Ping Liu, Bojun Chen, Roger Mailler, and Zhao-Wen Wang. Antidromic-rectifying gap junctions amplify chemical transmission at functionally mixed electrical-chemical synapses. *Nature communications*, 8:14818, 2017.
- [51] Qiang Liu, Philip B Kidd, May Dobosiewicz, and Cornelia I Bargmann. *C. elegans* awa olfactory neurons fire calcium-mediated all-or-none action potentials. *Cell*, 175(1):57–70, 2018.
- [52] Michael London and Michael Häusser. Dendritic computation. *Annu. Rev. Neurosci.*, 28: 503–532, 2005.
- [53] Nateri K Madavan. Multiobjective optimization using a pareto differential evolution approach. In *Proceedings of the 2002 Congress on Evolutionary Computation. CEC’02 (Cat. No. 02TH8600)*, volume 2, pages 1145–1150. IEEE, 2002.
- [54] Thomas Maertens, Eckehard Schöll, Jorge Ruiz, and Philipp Hövel. Multilayer network analysis of *c. elegans*: Looking into the locomotory circuitry. *Neurocomputing*, 427:238–261, 2021.
- [55] Eve Marder and Adam L Taylor. Multiple models to capture the variability in biological neurons and networks. *Nature neuroscience*, 14(2):133–138, 2011.
- [56] Henry Markram, Eilif Muller, Srikanth Ramaswamy, Michael W Reimann, Marwan Abdellah, Carlos Aguado Sanchez, Anastasia Ailamaki, Lidia Alonso-Nanclares, Nicolas Antille, Selim Arsever, et al. Reconstruction and simulation of neocortical microcircuitry. *Cell*, 163 (2):456–492, 2015.
- [57] Stefano Masoli, Martina F Rizza, Martina Sgritta, Werner Van Geit, Felix Schürmann, and Egidio D’Angelo. Single neuron optimization as a basis for accurate biophysical modeling: the case of cerebellar granule cells. *Frontiers in cellular neuroscience*, 11:71, 2017.
- [58] Jerry E Mellem, Penelope J Brockie, David M Madsen, and Andres V Maricq. Action potentials contribute to neuronal signaling in *c. elegans*. *Nature neuroscience*, 11(8):865, 2008.
- [59] Lois Naudin, Nathalie Corson, MA Aziz-Alaoui, Juan Luis Jiménez Laredo, and Thibaut Démare. On the modeling of the three types of non-spiking neurons of the *caenorhabditis elegans*. *International Journal of Neural Systems*, page S012906572050063X, 2020.
- [60] Robert O’Hagan, Martin Chalfie, and Miriam B Goodman. The *mec-4 deg/enac* channel of *caenorhabditis elegans* touch receptor neurons transduces mechanical signals. *Nature neuroscience*, 8(1):43, 2005.
- [61] Erick Olivares, Eduardo Izquierdo, and Randall Beer. A neuromechanical model of multiple network oscillators for forward locomotion in *c. elegans*. *BioRxiv*, page 710566, 2019.
- [62] Panayiota Poirazi and Athanasia Papoutsis. Illuminating dendritic function with computational models. *Nature Reviews Neuroscience*, pages 1–19, 2020.

- [63] Thomas E Portegys. Training sensory–motor behavior in the connectome of an artificial *c. elegans*. *Neurocomputing*, 168:128–134, 2015.
- [64] Kenneth Price, Rainer M Storn, and Jouni A Lampinen. *Differential evolution: a practical approach to global optimization*. Springer Science & Business Media, 2006.
- [65] Weiyi Qian et al. Adaptive differential evolution algorithm for multiobjective optimization problems. *Applied Mathematics and Computation*, 201(1-2):431–440, 2008.
- [66] Franciszek Rakowski, Jagan Srinivasan, Paul W Sternberg, and Jan Karbowski. Synaptic polarity of the interneuron circuit controlling *c. elegans* locomotion. *Frontiers in computational neuroscience*, 7:128, 2013.
- [67] Daniel Ramot, Bronwyn L MacInnis, and Miriam B Goodman. Bidirectional temperature-sensing by a single thermosensory neuron in *c. elegans*. *Nature neuroscience*, 11(8):908, 2008.
- [68] Alan Roberts and Brian MH Bush. *Neurons without impulses: their significance for vertebrate and invertebrate nervous systems*, volume 6. Cambridge University Press, 1981.
- [69] Tea Robič and Bogdan Filipič. Differential evolution for multiobjective optimization. In *International conference on evolutionary multi-criterion optimization*, pages 520–533. Springer, 2005.
- [70] Indrajit Saha, Ujjwal Maulik, and Dariusz Plewczynski. A new multi-objective technique for differential fuzzy clustering. *Applied Soft Computing*, 11(2):2765–2776, 2011.
- [71] Indrajit Saha, Ujjwal Maullik, Michal Łukasik, and Dariusz Plewczynski. Multiobjective differential evolution: a comparative study on benchmark problems. In *Man-Machine Interactions 3*, pages 529–536. Springer, 2014.
- [72] Kazumi Sakata and Ryuzo Shingai. Neural network model to generate head swing in locomotion of *caenorhabditis elegans*. *Network: Computation in Neural Systems*, 15(3):199–216, 2004.
- [73] Bert Sakmann. *Single-channel recording*. Springer Science & Business Media, 2013.
- [74] Gopal P Sarma, Chee Wai Lee, Tom Portegys, Vahid Ghayoomie, Travis Jacobs, Bradley Alicea, Matteo Cantarelli, Michael Currie, Richard C Gerkin, Shane Gingell, et al. Openworm: overview and recent advances in integrative biological simulation of *caenorhabditis elegans*. *Philosophical Transactions of the Royal Society B*, 373(1758):20170382, 2018.
- [75] Rahul Sarpeshkar. Analog versus digital: extrapolating from electronics to neurobiology. *Neural computation*, 10(7):1601–1638, 1998.
- [76] Rainer Storn and Kenneth Price. Differential evolution—a simple and efficient heuristic for global optimization over continuous spaces. *Journal of global optimization*, 11(4):341–359, 1997.
- [77] Greg J Stuart and Nelson Spruston. Dendritic integration: 60 years of progress. *Nature neuroscience*, 18(12):1713–1721, 2015.
- [78] Balázs Szigeti, Pádraig Gleeson, Michael Vella, Sergey Khayrulin, Andrey Palyanov, Jim Hokanson, Michael Currie, Matteo Cantarelli, Giovanni Idili, and Stephen Larson. Openworm: an open-science approach to modeling *caenorhabditis elegans*. *Frontiers in computational neuroscience*, 8:137, 2014.

- [79] Du-Juan Wang, Feng Liu, and Yaochu Jin. A multi-objective evolutionary algorithm guided by directed search for dynamic scheduling. *Computers and Operations Research*, 79:279–290, 2017.
- [80] Stephen R Wicks, Chris J Roehrig, and Catharine H Rankin. A dynamic network simulation of the nematode tap withdrawal circuit: predictions concerning synaptic function using behavioral criteria. *Journal of Neuroscience*, 16(12):4017–4031, 1996.
- [81] Allan R Willms, Deborah J Baro, Ronald M Harris-Warrick, and John Guckenheimer. An improved parameter estimation method for hodgkin-huxley models. *Journal of computational neuroscience*, 6(2):145–168, 1999.
- [82] Feng Xue, Arthur C Sanderson, and Robert J Graves. Pareto-based multi-objective differential evolution. In *The 2003 Congress on Evolutionary Computation, 2003. CEC'03.*, volume 2, pages 862–869. IEEE, 2003.